Technical feasibility of integrating 7 T anatomical MRI in image-guided radiotherapy of glioblastoma

Magn Reson Mater Phy (2016) 29:591–603
DOI 10.1007/s10334-016-0534-7

RESEARCH ARTICLE

Technical feasibility of integrating 7 T anatomical MRI in image-guided radiotherapy of glioblastoma: a preparatory study

Inge Compter[1] · Jurgen Peerlings[1,2] · Daniëlle B. P. Eekers[1] · Alida A. Postma[2] · Dimo Ivanov[3] · Christopher J. Wiggins[4] · Pieter Kubben[5] · Benno Küsters[6,7] · Pieter Wesseling[7,8] · Linda Ackermans[5] · Olaf E. M. G. Schijns[5] · Philippe Lambin[1] · Aswin L. Hoffmann[1,9,10]

Received: 2 December 2015 / Revised: 3 February 2016 / Accepted: 10 February 2016 / Published online: 30 March 2016

Abstract
Objectives The use of 7 Tesla (T) magnetic resonance imaging (MRI) has recently shown great potential for high-resolution soft-tissue neuroimaging and visualization of microvascularization in glioblastoma (GBM). We have designed a clinical trial to explore the value of 7 T MRI in radiation treatment of GBM. For this aim we performed a preparatory study to investigate the technical feasibility of incorporating 7 T MR images into the neurosurgical navigation and radiotherapy treatment planning (RTP) systems via qualitative and quantitative assessment of the image quality.
Materials and methods The MR images were acquired with a Siemens Magnetom 7 T whole-body scanner and a Nova Medical 32-channel head coil. The 7 T MRI pulse sequences included magnetization-prepared two rapid acquisition gradient echoes (MP2RAGE), T2-SPACE, SPACE-FLAIR and gradient echo sequences (GRE). A pilot study with three healthy volunteers and an anthropomorphic 3D phantom was used to assess image quality and geometrical image accuracy.
Results The MRI scans were well tolerated by the volunteers. Susceptibility artefacts were observed in both the cortex and subcortical white matter at close proximity to air-tissue interfaces. Regional loss of signal and contrast could be minimized by the use of dielectric pads. Image transfer and processing did not degrade image quality. The system-related spatial uncertainty of geometrical distortion-corrected MP2RAGE pulse sequences was $\leq$2 mm.
Conclusion Integration of high-quality and geometrically-reliable 7 T MR images into neurosurgical navigation and RTP software is technically feasible and safe.

Keywords Ultra-high field MRI · Radiotherapy · Treatment planning · Glioblastoma · Geometrical distortion

I. Compter and J. Peerlings contributed equally to this work.

✉ Inge Compter
inge.compter@maastro.nl

[1] Department of Radiation Oncology (MAASTRO CLINIC), GROW-School for Oncology and Developmental Biology, Maastricht University Medical Centre, Maastricht, The Netherlands

[2] Department of Radiology, Maastricht University Medical Center, Maastricht, The Netherlands

[3] Department of Cognitive Neuroscience, Faculty of Psychology and Neuroscience, Maastricht University, Maastricht, The Netherlands

[4] Scannexus, Maastricht, The Netherlands

[5] Department of Neurosurgery, Maastricht University Medical Center, Maastricht, The Netherlands

[6] Department of Pathology, Maastricht University Medical Center, Maastricht, The Netherlands

[7] Department of Pathology, Radboud University Medical Center, Nijmegen, The Netherlands

[8] Department of Pathology, VU University Medical Center, Amsterdam, The Netherlands

[9] Institute of Radiooncology, Helmholtz-Zentrum Dresden-Rossendorf, Dresden, Germany

[10] Department of Radiation Oncology, University Hospital Carl Gustav Carus at the Technische Universität Dresden, Dresden, Germany

Introduction

Glioblastoma (GBM) is the most common type of primary brain tumour, with a peak incidence in the 6th and 7th decade of life. Patients with a GBM have an extremely poor prognosis with a median overall survival of 14.6 months [1]. The main goals of surgery are verification of histological diagnosis and reduction of any mass effect. A complete resection is nearly impossible because of the infiltrative nature of this disease and its spread along white matter tracts [2]. Therefore, patients up to 70 years old with a good performance status are treated with adjuvant radiotherapy in combination with temozolomide to delay local tumour recurrence and increase overall survival. Radiotherapy usually consists of conventionally fractionated regimens, delivering a dose of 59.4–60 Gy in 6–7 weeks. Computed tomography (CT) images (1 mm slices) are commonly used for radiation therapy planning (RTP) because of the excellent spatial quality (i.e., no geometrical distortions) and the electron density information that is required for accurate dose calculations. In current RTP practice for GBM, contrast-enhanced (CE) CT images are co-registered with 1.5 or 3 T magnetic resonance (MR) images because the latter offer superior soft-tissue contrast over CT images. Subsequently, a gross tumour volume (GTV) is delineated based on the resection cavity and any residual disease visible on CE T_1-weighted MRI scans. According to European guidelines, a 2–3 cm isotropic margin is added to the GTV to encompass any non-enhancing tumour tissue and to establish the clinical target volume (CTV) [3]. This margin is based on the fact that over 80 % of recurrences occur within 2 cm of the GTV [4, 5]. However, the isotropic margin does not take into account spatially varying tumour-growth dynamics in different brain tissues and tumour spread along white matter tracts, which evidently results in needlessly damaging healthy cells while leaving viable malignant cells outside the CTV [6]. A planning target volume (PTV) margin is added to account for systematic and random errors such as setup errors, inter and intrafraction motion, but also uncertainty in image registration and delineation. Current clinically available MRI techniques are unable to adequately visualize tumour spread throughout the brain. Ultra-high field (UHF) (>3 T) MRI might be able to overcome these limitations, because of the increased signal-to-noise ratio (SNR) and susceptibility effects, which allow for an increased spatial resolution and better contrast in comparison to clinically-used 1.5 and 3 T MRI. However, the potential of UHF MRI for RTP of GBM has not been investigated so far.

With regard to neurosurgical planning, UHF MRI may benefit image-guided biopsies through identification of increased vascularity suggestive for tumour grade. Endothelial proliferation and increased microvascularization are key features for the diagnosis of GBM according to the WHO criteria [7]. An increase in susceptibility effects, as seen with UHF MRI in comparison to lower field strengths, results in novel contrast mechanisms on quantitative T_2*-weighted images by which microvascularization with a vessel diameter as small as 100 μm can be visualized [8–11].

We therefore hypothesize that 7 T MRI allows for better delineation of the GTV of GBM due to improved visualization of microvascularization. We have designed a future clinical study to investigate this, which includes a 7 T-image-guided biopsy and RTP (clinicaltrials.gov NCT 02062372). In this paper we describe the technical aspects of the preparatory work for this clinical trial. If 7 T MR images are to be used for neurosurgical and RTP purposes, a high spatial reliability is required. Although 7 T MRI may hold promise for inclusion into neurosurgical navigation and RTP, it also presents technical challenges such as inhomogeneity of the transmit B_1-field, an increased specific absorption rate (SAR), and geometrical distortions caused by increased static magnetic field (B_0) inhomogeneity, tissue susceptibility differences, and chemical shift effects [12–14]. In order to measure the geometric accuracy, a phantom study was conducted to quantify system-related geometrical image distortions. Furthermore, a pilot study with healthy volunteers was conducted to investigate whether the 7 T MRI images meet the requirements for clinical application in RTP, such as visualization of brain anatomy structures on different sequences, differences in scanning times and patient tolerability of the scan. In this paper we report on the challenges and pitfalls we encountered in the preparation of our clinical study, and present solutions we developed to quantify the system-related geometrical image distortions and to optimize 7 T MRI scanning protocols, as well as the image transfer and processing workflow.

Materials and methods

Pilot study

A pilot study with healthy volunteers was conducted to assess the image quality in terms of field inhomogeneity and susceptibility artefacts and to optimize the pulse sequences and scanning protocols for RTP purposes. Prior to the 7 T MRI scan all volunteers received detailed information regarding the purpose of the study and possible temporary sensory side effects due to the applied magnetic field. Written informed consent was obtained prior to participation. A total of three volunteers were recruited: two

females (26 and 37 years old) and one male (29 years old). Subjects filled out a safety questionnaire prior to the scan regarding e.g. medication, claustrophobia, and metallic objects, and were instructed not to move during the scanning procedure. They were positioned in a head-first supine position and dielectric pads were fixed on both sides of the subject's head next to the temporal lobes after which the head coil was placed. The dielectric pads contained a 25 % suspension of barium titanate in deuterated water and were used to locally increase the transmit B_1^+ field to improve its homogeneity across the brain [15]. Cushions were placed under the knees to provide extra comfort.

Phantom study

Geometrical distortion is a recognized problem in anatomical MRI, sometimes resulting in pixel shifts of several millimetres, which is detrimental for application of MRI in image-guided interventions in neurosurgery and radiotherapy. Geometric inaccuracies originate from system- (i.e., B_0-inhomogeneity, gradient field nonlinearity) or object- (i.e., chemical shift, susceptibility effects) related causes, and can to some extent be corrected for by manufacturer-developed distortion correction methods and shimming procedures. As magnetic field inhomogeneity, chemical shift, and susceptibility are proportional to B_0, the spatial inaccuracy increases with higher magnetic field strength. Hence, estimation of the geometrical distortion is essential before 7 T MRI can be integrated into image-guided interventions.

For the assessment of system- and sequence-related geometrical image distortions, we used a dedicated 3D anthropomorphic skull phantom (CIRS Model 603A, Computerized Imaging Reference Systems, Inc., Norfolk, Virginia, United States; Figs. 1, 2a, b). This phantom is made up of a plastic-bone tissue substitute and soft-tissue equivalent material consisting of a water-based polyacrylamide (Zerdine®, CIRS). The entire phantom is encased in a clear vacuum-formed plastic shell to protect the gel from desiccation. The cranial portion of the skull volume is filled with an orthogonal 3D grid of 3 mm diameter rods (reinforced nylon) spaced 15 mm apart. The maximum 3D grid-size is 15 × 12 × 13.5 cm^3 (AP × LR × SI), resulting in 436 measurable grid-intersection points. Since nylon shows magnetic susceptibility properties similar to water (i.e., difference in susceptibility <3 ppm), the phantom rods are expected not to induce artefacts and image abnormalities in either spin-echo or gradient-echo sequences [16]. The phantom was placed in an ABS vacuum-formed cradle to ensure reproducible placement within the scanner. Both CT and 7 T MRI images were acquired in order to compare the geometrical distortions of both imaging modalities.

Fig. 1 Anthropomorphic skull phantom CIRS 603A. Source: Computerized Imaging Reference Systems, Inc (CIRS), viewed 22 November 2015 http://www.cirsinc.com/products/modality/99/mri-distortion-phantom-for-srs/

Image acquisition

For the phantom study, CT images (SOMATOM Sensation 10, Siemens Healthcare, Erlangen, Germany) were acquired at the MAASTRO CLINIC with a 1-mm slice thickness, 306 slices, 50 × 50 cm^2 field of view, 140 kV, 400 mAs.

For the pilot and phantom study, MR images were acquired at the Scannexus facility with a 7 T whole-body scanner (Magnetom 7 T, Siemens Healthcare, Erlangen, Germany) in combination with a 32-channel head coil (Nova Medical, Wilmington, United States). Pulse sequences included multi-echo gradient echo (GRE), magnetization-prepared rapid gradient-echo (MP2RAGE) [17], T2-sampling perfection with application optimized contrasts using different flip-angle evolution (T2-SPACE), and sampling perfection with application optimized contrasts using different flip-angle evolution FLAIR (SPACE-FLAIR) (Table 1).

7 T MRI sequence selection and optimization

Sequences were selected to highlight differences in tissue contrast [18] and visualize microvascularization [9, 10]. A standard method for obtaining T_1-contrast is the MPRAGE (magnetization-prepared rapid gradient-echo) sequence, which provides good grey-white matter contrast [19]. Due to inhomogeneities in both the transmit and receive radiofrequency (RF) fields, a newer variant (MP2RAGE) was

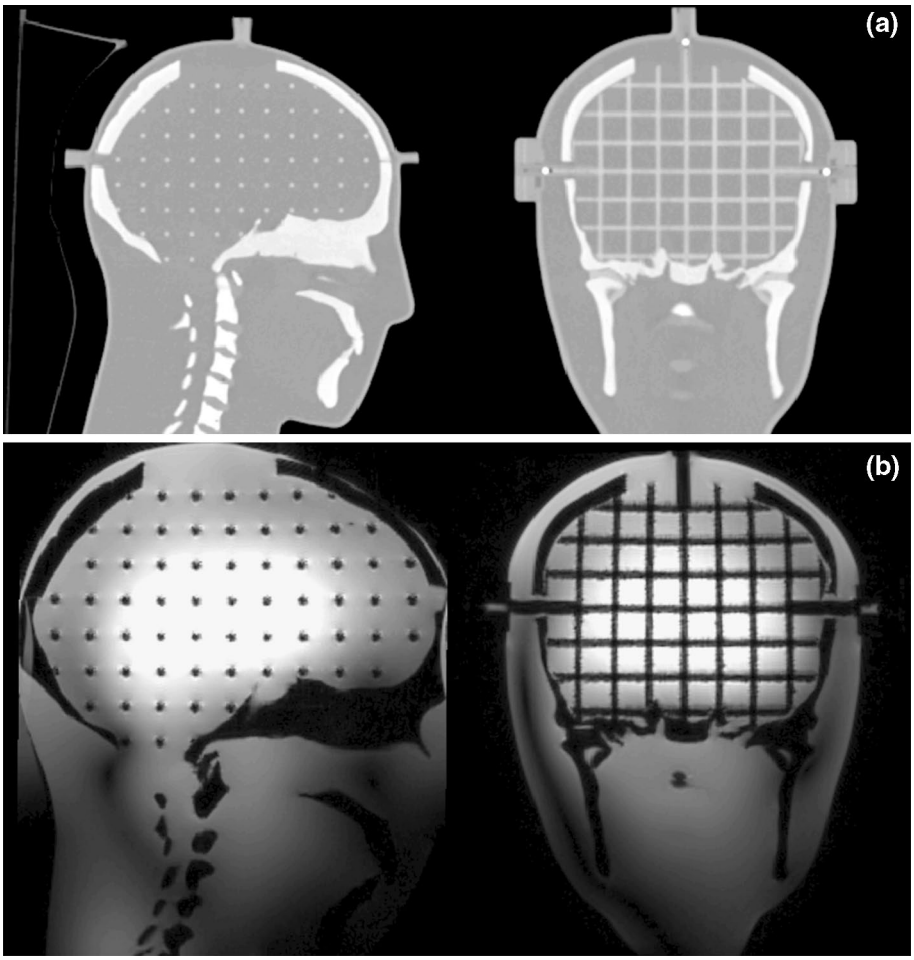

Fig. 2 Sagittal and coronal slice of the CIRS 603A phantom on CT (**a**), and 7 T MRI (**b**) scan

Table 1 Scan parameters per 7 T MRI pulse sequence

	MP2RAGE	SPACE	SPACE-FLAIR	GRE
Repetition time TR (ms)	5000	4000	8000	33
Echo time TE (ms)	2.5	283	302	2.5
Inversion time (ms)	TI1 900 TI2 27500	N/A	2330	N/A
Field of view (mm)	223 × 223	192 × 192	193 × 206	160 × 223
Nominal flip angle (°)	5 and 3	Variable	Variable	11
Acquisition matrix (pixel)	0\320\320\0	0\320\320\0	0\256\240\0	0\320\320\0
Bandwidth (Hz/pixel)	248	372	383	290
Slices (*n*)	240	288	208	208
Slice thickness (mm)	0.7	0.6	0.8	0.7
Acquisition time (min)	8.02	7.50	10.58	8.33

used that generates two different images at different inversion times and allows for self-correction of the bias fields [20].

The MP2RAGE sequence with optimized TR-FOCI inversion pulse was chosen for T_1-weighted imaging instead of the MPRAGE because received bias field could be corrected online (Fig. 3a) [21–24]. In particular, the T_1-weighted images were obtained as the ratio of the two volumes acquired at different inversion times (INV1 and INV2), which minimizes the effect of B_1-variations through space. A quantitative T_1-map was calculated online by linear interpolation of the INV1 and INV2 images [17]. An optimized four-echo GRE was used instead of the typical single-echo GRE with a long echo time in order to correct

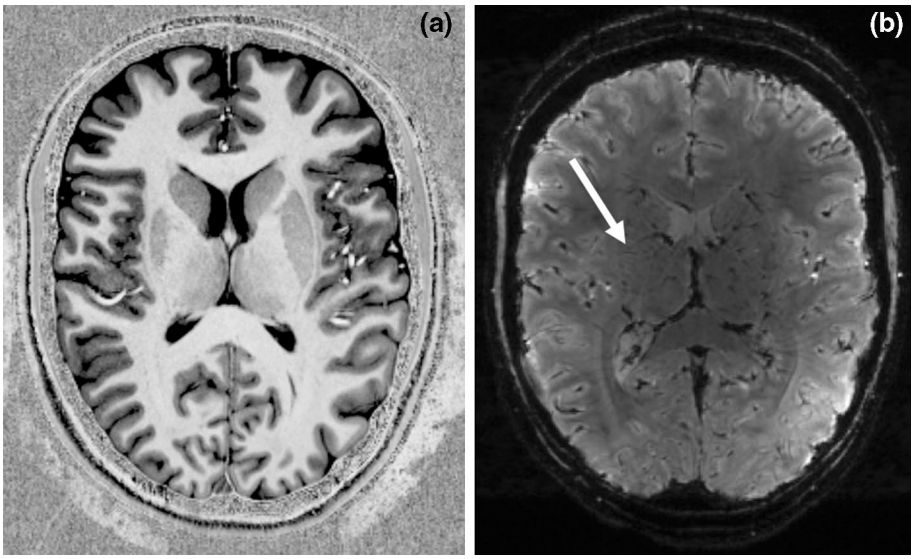

Fig. 3 Axial slices of 7 T MRI T_1-weighted image from MP2RAGE (**a**), and T_2*-weighted image from GRE (**b**) of a healthy volunteer. *White arrow* exemplifies the fine vascularisation detail that is observed

for B_1-inhomogeneities and obtain quantitative T_2*-images (Fig. 3b).

T_2-weighted imaging using standard Turbo Spin Echo sequences becomes increasingly difficult at UHF due to a relatively high SAR induced by multiple 180° refocussing pulses [25]. For this reason, a technique involving the use of a tailored RF flip angle train was used (T2-SPACE) to obtain T_2-like contrast [26–28]. This same technique was also used as the basis for a FLAIR-type contrast (SPACE-FLAIR), where an inversion pulse, with inversion time of 2330 ms, was added to null fluid signals. For both T_2-weighted sequences, a Works-In-Progress package [WIP 692] from Siemens was used and parameters were optimised to obtain excellent contrast, with reference to standard clinical imaging. All images were reconstructed with and without manufacturer-developed correction procedures to restore gradient uniformity.

Image transfer and processing workflow

Since MAASTRO CLINIC and Scannexus each operate independently from the Maastricht University Medical Center (MUMC), a dedicated inter-institutional imaging workflow was developed to be able to collaboratively share the 7 T MR images acquired at Scannexus with the department of Neurosurgery at MUMC and the Radiation Oncology department at MAASTRO CLINIC. Our solution comprised a cloud-based medical image sharing environment (Quentry, version 3.0, Brainlab AG, Feldkirchen, Germany) to upload the 7 T MR images into the neurosurgical cranial navigation software (iPlan Net, version 3.6, Brainlab AG, Feldkirchen, Germany) that will be used to obtain the biopsy specimen for the future clinical study. The MiTools software package was used to generate quantitative T_2*-maps from the multi-echo GRE images (http://od1n.sourceforge.net/). The 7 T MRI scans were imported directly as DICOM files into the radiation treatment planning system (Eclipse version 11, Varian, Palo Alto, United States of America) from the Scannexus facility.

Image quality assessment

Qualitative image analysis

During a multi-disciplinary session, a physicist, neuro-radiologist, and radiation oncologist visually verified that the MR image quality was warranted after acquisition, transfer and processing of the images. Image quality was assessed by evaluating the images of all three volunteers on the MR scanner console and within the neurosurgical navigation and RTP software. The MP2RAGE, T2-SPACE, and SPACE-FLAIR sequences were visually evaluated by an experienced neuro-radiologist for SNR, visualisation of the cerebral lobes, depiction of grey-white matter, basal ganglia, ventricles, and CSF around the brain. Each of these factors was classified on a scale of 1–4 (1, excellent; 2, good; 3, marginal, but still diagnostic; 4, non-diagnostic). The GRE images were not assessed, as these images were post-processed in order to obtain quantitative T_2*-images.

Quantitative image analysis: geometrical image distortion

To assess the geometrical reliability of the 7 T MR images, two clinically-relevant pulse-sequences (GRE and MP2RAGE) were used to acquire images of the phantom, both with and without automatic geometric distortion correction. Unfortunately, it was found that the distortion correction processing was not compatible with the

multi-echo data, causing severe artefacts. For this reason, only the data from the MP2RAGE is presented. We aim to resolve this incompatibility in future clinical studies. The GRE and MP2RAGE sequences were selected to assess sequence-related geometrical image distortions, as they will be primarily used for GTV delineation in the clinical study.

Next, the 3D coordinates of all 436 grid-intersection points were acquired after manual processing of the respective CT and MR images in Eclipse. The coordinates of the reference points were deduced from the phantom's known geometry.

Two methods were used to measure the geometrical distortion at different levels of sophistication. The first method was used to assess the overall image distortion using an in-house developed MATLAB script (R2014b, MathWorks Inc, Natick, USA). All unique pairs of grid-intersection point coordinates were generated, from which the Euclidean distance was subsequently determined, and absolute differences in distance were calculated between the reference (i.e., phantom-based) and measured (i.e., image-based) distances. In a second method, Euclidean distances were measured between a fixed reference point located at the magnetic field isocenter, and all other grid-intersection points in the image, and compared to corresponding distances within the reference frame. Hence, a measure of the geometrical dispersion relative to the magnetic field isocenter was obtained. Both methods were applied to the CT and MRI scans. The overall geometric distortion was quantified by the global mean absolute deviation (MAD_{global}) and its standard deviation (SD), while geometrical dispersion relative to the isocenter was quantified by local mean absolute deviation (MAD_{local}) and its SD:

$$MAD_{global}=\frac{1}{i}\sum_{i}|D_{ref}-D_m|_i$$

$$MAD_{local}=\frac{1}{i}\sum_{i}|D_{ref}-D_{isoc}|_i,$$

where D_{ref} represents the Euclidian distance between reference points, D_m is the measured distance between image-based grid points, and D_{isoc} is the measured distance between the magnetic field isocenter and surrounding grid points. For each measurement within a cluster of unique distances i, the MAD is then calculated as the average of the absolute difference in Euclidian distances.

Given the MAD and its standard deviation (SD), a 95 % confidence interval (Δ) was calculated as:

$$\Delta = \pm(MAD + 2SD).$$

Based on this confidence interval, a maximum acceptable tolerance level of 2.0 mm was defined. When MAD >1.0 mm and $|\Delta| > 2.0$ mm, the level of geometric deviation between the measured and reference dimensions were considered unacceptable.

Results

Image acquisition

The duration of the scanning sessions for the volunteers was 50 min. All three volunteers reported slight vestibular effects while being moved in and out of the magnetic field. One of the volunteers reported twitching of the nose tip during the scanning procedure. No other clinically relevant sensory effects were reported. The duration of the scanning session for the phantom was up to 150 min, as it was scanned with the same sequences as the volunteers in three orthogonal planes (axial, sagittal, coronal).

Image quality

Qualitative image analysis

Images acquired with MP2RAGE (Fig. 3a), T2-SPACE, and SPACE-FLAIR sequences all showed good to

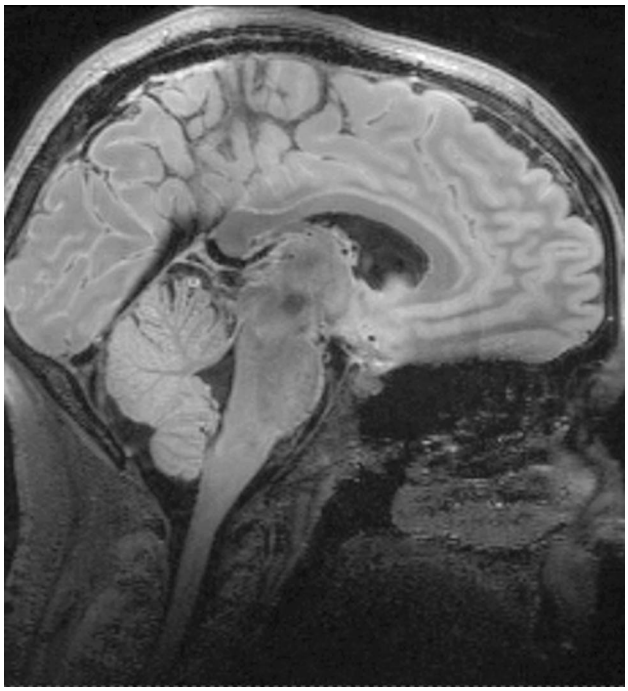

Fig. 4 Sagittal 7 T MRI SPACE-FLAIR image of a healthy volunteer, showing increased geometrical distortion near the skull base, the ventral part of the temporal cortices, and the orbito-frontal cortex

excellent SNR and visualization of the frontal and parietal lobes. Furthermore, there was a good to excellent reproduction of the ventricles and CSF surrounding the brain. All sequences showed marginal to good SNR and visualization of the cerebellum. The reproduction of CSF around the cerebellum was good, except for on T2-SPACE where it was judged to be non-diagnostic to marginal. All sequences demonstrated non-diagnostic to marginal image quality for SNR, visualization of the cerebral lobes, depiction of grey-white matter and ventricles and depiction of CSF around the brain at the frontobasal and temporal lobes. This decrease in image quality was primarily caused by a decrease in signal and susceptibility artefacts near the skull base (Fig. 4). The reproduction of the basal ganglia was good to excellent on T2-SPACE and MP2RAGE, respectively, but was considered marginal in one of the volunteers on SPACE-FLAIR due to flow-artefacts. The visualization of the cerebral vessels was good to excellent on both T2-SPACE and MP2RAGE and considered marginal to good on the SPACE-FLAIR. There was a signal inhomogeneity present in the T2-SPACE and SPACE-FLAIR images in both the medial–lateral and anterior-posterior direction. Moreover, the T2-SPACE showed a signal drop at both the skull base and the temporal lobes. Ghosting artefacts were anteriorly and posteriorly present in the T2-SPACE and SPACE-FLAIR. These may be the result of the relatively high amount of image acceleration used (2×2 GRAPPA) and it may be possible to reduce these artefacts through enhanced image reconstruction. In addition, flow-artefacts were observed near major intra-cranial vessels such as the carotid and basillary arteries. Image transfer and processing did not visually degrade the image quality.

Quantitative image analysis: geometrical image distortion

Global distortion method Based on the 436 reference points of the 3D grid, 95,266 unique distances between grid-intersection points were calculated and paired into 100 unique distance clusters, ranging from 15 to 164.32 mm. The corresponding image-based distances were paired into the same clusters for calculating MAD_{global}.

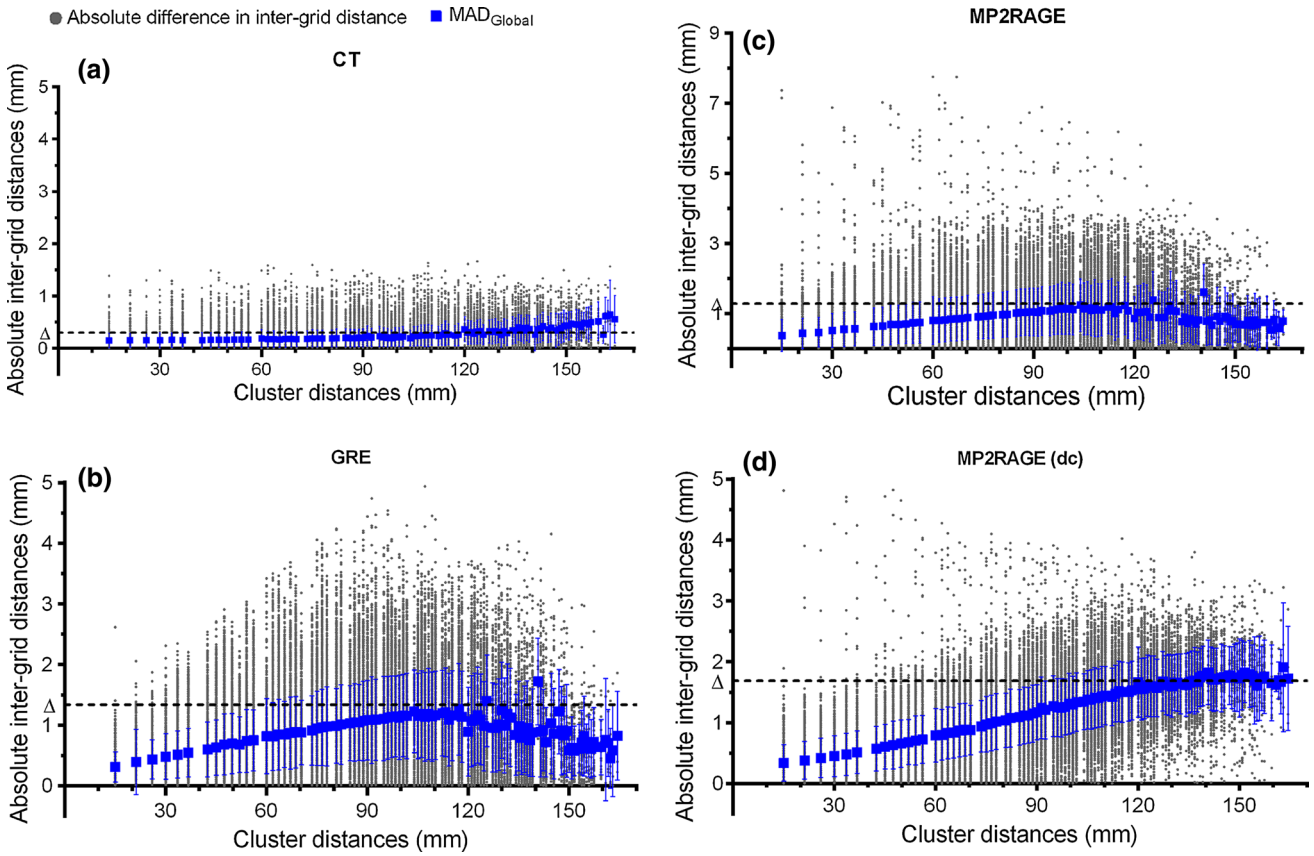

Fig. 5 Absolute inter-grid distances (*grey dot*) measured within CT (**a**), distortion-uncorrected GRE images (**b**), distortion-uncorrected MP2RAGE images (**c**), and distortion-corrected MP2RAGE (**d**) relative to the possible cluster distances in mm. The overall geometric distortion was quantified by MAD_{global} (*blue square*) and its standard deviation. The 95 % confidence interval (Δ) is shown as the *dotted line*

Figure 5 presents the absolute difference between phantom- and image-based distances within each cluster, as well as the MAD_{global} of that cluster. The global geometric distortion within the MR-images is more pronounced than in CT images. However, CT is not completely free of distortion errors with average MAD_{global} of 0.20 mm (SD $\pm$ 0.05 mm) (Fig. 5a). The GRE and MP2RAGE sequences present MAD_{global} ranges of 0.31–1.35 and 0.38–1.62 mm, respectively, in distortion-uncorrected images (Fig. 5b, c). Furthermore, the measured differences were less consistent in MP2RAGE images with various outliers above the 95 % confidence interval ($\Delta = 1.29$ mm), mostly at small intergrid distances. In the distortion-corrected MP2RAGE images, relatively similar patterns of MAD_{global} could be noted (Fig. 5d) with values ranging from 0.34–1.91 mm ($\Delta = 1.68$ mm). Table 3 provides a clear overview of MAD ranges, average MAD, and MAD confidence intervals per selected image.

Local distortion method Figure 6 shows the geometrical dispersion relative to the isocenter (MAD_{local}) and illustrates modality-and sequence-dependent distortion effects and the quality of the MR-distortion correction methods. In CT-images, MAD_{local} ranges from 0.06–0.27 mm, indicating small spatial deviations. In the distortion-uncorrected 7 T MR images, MAD_{local} ranges from 0.28–1.31 mm ($\Delta = 0.99$ mm) in GRE images and 0.26–1.46 mm ($\Delta = 1.04$ mm) in MP2RAGE images. In the distortion-corrected MR-images, MAD_{local} ranges from 0.22–1.82 mm ($\Delta = 1.56$ mm) in MP2RAGE images. The value for MAD_{local} is observed with increasing distance from the magnetic field isocenter, with a maximum of 1.82 mm near the edges of the phantom. At equal distance from the isocenter, geometric distortion was found to be anisotropic. For distortion-corrected MP2RAGE images, major spatial displacement could be noted in the superior-inferior (SI) direction (e.g., 0.82 mm at 45 mm isocenter distance).

Based on the average MAD-values for CT and 7 T MRI, both modalities present tolerable levels of geometrical image distortion with average MAD $\leq$ 1.0 mm and $\Delta \leq 2.0$ mm (Tables 2, 3). However, MAD_{global} and MAD_{local} of larger cluster distances often exceed this tolerance limit. For corrected MP2RAGE images, MAD_{global} was >1.0 mm for intergrid distances >77.9 mm. MAD_{local} measurements in distortion-corrected MP2RAGE images was <1.0 mm up until 68.7 mm from the isocenter.

Discussion

This paper reports on the preparatory work for our clinical study to integrate 7 T MR images into neurosurgical navigation and RTP systems. It includes a pilot study with healthy volunteers and a phantom study. The volunteers in our pilot study reported limited side effects of the 7 T MRI. Similar to other studies on UHF MRI, mainly transient vestibular effects were noted [29, 30]. In our study these effects were only present during a change in table position. The cause of transient vertigo and dizziness is not yet fully understood, but magnetic stimulation of the ear's labyrinth has been suggested [31].

There are currently still a few shortcomings in image quality that need to be resolved before clinical implementation of UHF MRI. Although image quality in our study was good to excellent in the frontal and parietal lobes, all sequences demonstrated a non-diagnostic to marginal image quality for all evaluated parameters at the frontobasal and temporal lobes. This is a well-known issue for UHF-MRI and is generally caused by a decrease in signal and susceptibility artefacts near the skull base. As a consequence, patients with tumours near the skull base will be excluded from our clinical trial.

Many researchers have been working on improving the inversion contrast in MPRAGE, particularly trying to reduce the sensitivity to off-resonance and RF inhomogeneity effects [19]. RF transmit technology is a very active research field within UHF MRI, and better transmitter designs may become available. The application of dielectric pads improves the transmit field homogeneity, which in our case ensured obtaining sufficient signal from the temporal regions [15, 32]. Concurrently, the application of dielectric pads also affects the receive B_1 field and can lead to signal increases in their immediate vicinity. Image intensity inhomogeneities of this kind are also typical for multi-channel RF receiver coils. They can be circumvented by image post-processing techniques such as division by an image with the appropriate weighting or by model fitting of at least two images differing by a single parameter [24]. The latter approach is utilized when generating the T_2*-maps from the multi-echo GRE data and T_1-maps from the MP2RAGE data, whereas the former approach is used to obtain the MP2RAGE T_1-weighted images. It is worth mentioning that the inversion pulse of the MP2RAGE sequence has been specifically designed to deliver homogeneous T_1-contrast across the whole brain despite B_1-inhomogeneities [22].

Yet further gains may be possible through the use of parallel transmit (pTx) technology, where 8 or 16 separate elements may be combined to produce a more uniform or targeted excitation. However, the use of such systems involves significant additional experimental setup (e.g., more complicated RF coils and pre-scans to determine per-subject transmit patterns, etc.), which may limit the applicability to patients. Additionally, SAR considerations are significantly more complicated in a pTx setup, as different excitation patterns will produce different SAR values within the

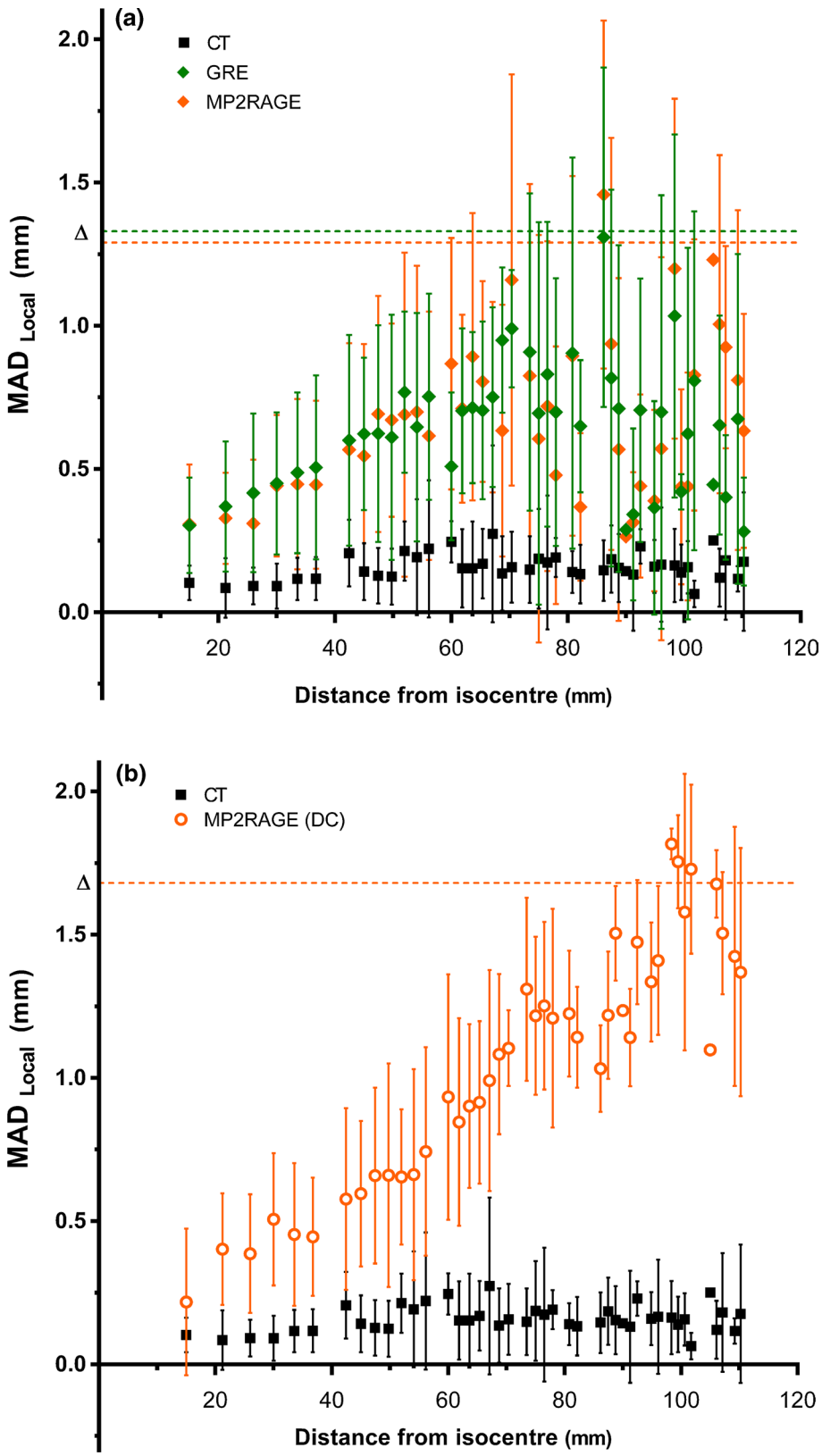

Fig. 6 Geometric dispersion relative to the magnetic field isocenter, quantified by MAD_{local} and its standard deviation within CT (*black square*) and distortion-uncorrected 7 T MR images **a** acquired with GRE (*green diamond*) and MP2RAGE (*orange diamond*) pulse sequences. Measured MAD_{local} values for CT and distortion-corrected 7 T MR images **b** acquired with MP2RAGE (*orange circle*) pulse sequence are shown relative to the distance

Table 2 Geometric distortion measures for CT

	MAD_{global} (mm)			MAD_{Local} (mm)		
	Range	Mean ± SD	Δ	Range	Mean ± SD	Δ
CT	0.14–0.64	0.20 ± 0.05	0.30	0.06–0.27	0.16 ± 0.04	0.24

Table 3 Geometric distortion measures for 7 T MRI

Sequence	DC	MAD_{global} (mm)			MAD_{Local} (mm)		
		Range	Mean ± SD	Δ	Range	Mean ± SD	Δ
GRE	No	0.31–1.35	0.88 ± 0.22	1.33	0.28–1.31	0.65 ± 0.17	0.99
MP2RAGE	No	0.38–1.62	0.88 ± 0.21	1.29	0.26–1.46	0.64 ± 0.20	1.04
MP2RAGE	3D	0.34–1.91	0.98 ± 0.35	1.68	0.22–1.82	0.85 ± 0.36	1.56

subject. While considerable progress has been made, there is still significant work required to implement this in clinical studies.

The phantom we used provides a realistic anthropomorphic scenario for CT and MRI to assess spatial distortion in 7 T MRI for clinical use. Although there is no standard procedure for assessing spatial distortion in 7 T MRI, AAPM and the Institute of Physics and Engineering in Medicine recommend measuring the distance between two selected points in the MR-image and calculating the deviation from the known distance [33, 34]. Based on these recommendations we assessed the geometrical image distortion using two different methods, MAD_{global} and MAD_{local}. We selected two variable points in the image for MAD_{global} assessment and selected one variable and one fixed point in the image (e.g., magnetic field isocenter) for MAD_{local} assessment [35, 36].

The assessment of geometrical distortion in our study is similar to the study by Cho et al. investigating the visualisation of targets for deep brain stimulation in Parkinson disease [13]. However, in the present study an updated version of the CIRS phantom was used. Furthermore, we did not consider CT as a reference standard and therefore did not co-register the CT to the MRI scan. Instead, the known geometry of the phantom was considered the reference.

Although no geometrical distortion was expected, we do report minimal distortion from the CT images. This was probably caused by measurement uncertainties from manually assessing the grid coordinates and was not found to be correlated to inter-grid distances or distances from the isocenter. For MRI however, overall geometric distortion increases exponentially with increasing distances between grid-intersection points. In uncorrected GRE and MP2RAGE images, a plateau-stage starts to manifest at 58 mm from the isocenter. Presumably, this plateau-stage could be attributed to the non-linearity of the gradient fields. Near the edges of the image, the assumed linear relationship between spin position and precession frequency in the local field is false, leading to a compression of the image. In distortion-corrected images, gradient uniformity was restored and as a result, the image was decompressed to its correct dimensions. Consequently, MP2RAGE sequences show a more linear increase of spatial deviation and higher MAD_{local} maxima are measured (Table 3). The larger range of MAD-values is related to the increase in measurable distance between grid-intersection points and the residual system-related geometrical distortion factors, such as eddy currents and B_0 inhomogeneity, which were not corrected for. Others have used a similar method, as applied in this study to estimate the reliability of stereotactic coordinates on 1.5 and 3 T MR images [37]. They reported a range of mean errors of 0.30–1.20 and 0.43–1.78 mm in T_1w-images at 1.5 and 3 T, respectively. For T_2w-images, they have shown ranges of 0.29–0.58 mm and 0.31–1.85 mm, respectively.

Geometric distortion can occur to different degrees depending on the imaging sequence parameter settings [38]. Differences in MAD_{local} between GRE and MP2RAGE could be attributed to differences in read-out bandwidth (rBW). With a lower rBW, more geometric distortion could be noted in the frequency-encoding or read-out direction. For MP2RAGE, a low rBW was used (250 Hz/pixel) for measurements in the SI read-out direction, while the read-out direction for GRE images was AP. To minimise this type of geometric distortion, a larger rBW could be selected, however, this in turn implies a loss in SNR. Increasing slice thickness could compensate for this loss in SNR, but is undesirable in clinical practise as resolution decreases.

Based on Figs. 5 and 6, we conclude that geometric distortion is anisotropic. When measuring local displacement at equal distances from the magnetic field isocenter, the geometric distortion correlates with the frequency-encoding direction. However, the exact quantification of

geometric distortion anisotropy was not investigated and will be analysed in future work. When interpreting MAD_{global} and MAD_{local}, it is important to note that the phantom used in this study describes the dimensions of a realistic human head. This implies that larger measurable distances from the isocenter could be measured in AP and SI direction than are possible in LR direction, leading to a possible misinterpretation of MAD_{global} and MAD_{local} and their respective SD.

Geometrical distortion, image registration, and delineation inaccuracies should all be taken into account while establishing the PTV margin for the clinical application of the 7 T MRI [39]. However, a larger PTV margin might be less relevant for RTP in GBM in which an isotropic CTV margin of 2–3 cm is added. An increase in PTV margin is highly detrimental for stereotactic radiosurgery, in which a very high radiation dose is given to a small volume of the brain. Manufacturer's distortion correction routines (i.e., gradient non-linearity correction and automated shimming) were applied to decrease geometric inaccuracies. However, Wang et al. showed that despite these measures, distortion can still be significantly present in UHF MR images [40]. As confirmed by our measurements (Fig. 5), the spatial deformation in geometrically corrected MR images is non-negligible for RTP purposes, especially for tumours located far from the magnetic field isocenter. This finding corresponds to the results obtained by other studies using a different phantom [12, 13]. Current use of MR images in radiotherapy planning requires co-registration to CT images, as information of electron density is needed for dose calculation. Although CT shows negligible geometric distortion, co-registration of CT and MR images introduces registration errors [41]. MRI-only-based treatment planning could provide an alternative to errors introduced through registration, but requires thorough investigation before clinical implementation [42].

Any technical and logistic challenges we encountered in the image transfer and processing workflow were primarily caused by the different image acquisition and processing platforms used at the different institutions and departments involved in this study, e.g. the 7 T MRI scanner at Scannexus, and neurosurgical and RTP software. Not all image data formats (e.g. NIfTi, xBrain) were compatible with these software systems. Fortunately, we could solve these problems by converting all image datasets into DICOM format and by using a cloud-based environment to collaboratively share the images. However, transfer and conversion of images could carry an inherent risk of data degradation and should be checked prior to clinical use.

The present study has several limitations and some factors that need to be considered when attempting to set up a similar study. First, the number of volunteers included in our pilot study was small. Moreover, sequence optimization was limited by the increase in SAR and scan duration and leaves room for future improvement. Second, unlike a human head, the anthropomorphic skull phantom did not contain any air cavities (i.e., sinuses) and only allowed assessment of the system-related geometrical distortion. Third, we only investigated geometrical distortion of 7 T MRI in comparison to CT and did not yet evaluate lower-field-strength MR images. Geometrical distortion in relation to 1.5 and 3 T field strengths will be addressed in a future study. Fourth, other hardware-related geometrical distortions such as eddy currents and B_0 inhomogeneity are not corrected, and remain present in the images. In general, B_0 inhomogeneity could be resolved with shimming and field map correction, although these corrections are mostly effective in EPI sequences [43, 44]. Finally, the distortion-corrected GRE images could not be assessed for geometrical distortion due to severe artefacts, therefore a comparison between distortion-corrected pulse sequences was not possible.

Several investigators suggested that the presence of microvasculature on UHF MRI may aid in improved identification of WHO tumour grade in GBM as compared to 3 T MRI [8, 10]. So far, these findings have not resulted in a systematic investigation of the potential value of 7 T MRI for improved neurosurgical navigation and target volume definition in RTP. Therefore, we aim to demonstrate the potential benefit of UHF MRI in identifying tumour infiltration for the delineation of GBM in our upcoming clinical study. This study is expected to open for inclusion in the first quarter of 2016. During the preparatory phase of the current study, image quality has significantly improved. However, further improvement of the image quality by reducing susceptibility artefacts in the frontobasal region and in the temporal lobe is required before clinical implementation.

Conclusion

Although the integration of high-quality and geometrically reliable 7 T anatomical MR images into neurosurgical navigation and RTP software is technically feasible and safe for the system and pulse sequences studied, image quality needs further improvement before it can be integrated into the clinical workflow. System-related geometrical distortions of the 7 T sequences studied are clinically acceptable for image co-registration with CT prior to radiotherapy and for direct use in neurosurgical procedures.

Acknowledgments This research was partially supported by the Brains Unlimited Pioneer Fund of the Limburg University Fund/SWOL. We would like to thank B.G. Baumert MD, PhD, MBA, for her support with the study concept. Furthermore, we would like to thank the Support Team at Scannexus, Margo van de Wetering and

Esther Steijvers, for their support in the acquisition and optimization of the 7 T MRI sequences.

Compliance with ethical standards

Conflict of interest Inge Compter has received a research grant from the Brains Unlimited Pioneer Fund of the Limburg University Fund/SWOL. Jurgen Peerlings declares that he has no conflict of interest Daniëlle B.P. Eekers declares that she has no conflict of interest Alida A. Postma declares that she has no conflict of interest Dimo Ivanov declares that he has no conflict of interest Christopher J. Wiggins declares that he has no conflict of interest Pieter Kubben declares that he has no conflict of interest Benno Küsters declares that he has no conflict of interest Pieter Wesseling declares that he has no conflict of interest Linda Ackermans declares that she has no conflict of interest Olaf E.M.G. Schijns declares that he has no conflict of interest Philippe Lambin declares that he has no conflict of interest Aswin L. Hoffmann declares that he has no conflict of interest.

Ethical approval The study was approved by the Medical Review Ethics Committee Maastricht UMC+ (Ethics code: 143018).

Research involving human participants All procedures performed in studies involving human participants were in accordance with the ethical standards of the institutional and/or national research committee and with the 1964 Helsinki declaration and its later amendments or comparable ethical standards.

Informed consent Informed consent was obtained from all individual participants included in the study. This trial is registered on clinicaltrials.gov (NCT02062372).

References

1. Stupp R, Hegi ME, Mason WP, van den Bent MJ, Taphoorn MJ, Janzer RC, Ludwin SK, Allgeier A, Fisher B, Belanger K, Hau P, Brandes AA, Gijtenbeek J, Marosi C, Vecht CJ, Mokhtari K, Wesseling P, Villa S, Eisenhauer E, Gorlia T, Weller M, Lacombe D, Cairncross JG, Mirimanoff RO (2009) Effects of radiotherapy with concomitant and adjuvant temozolomide versus radiotherapy alone on survival in glioblastoma in a randomised phase III study: 5-year analysis of the EORTC-NCIC trial. Lancet Oncol 10(5):459–466. doi:10.1016/S1470-2045(09)70025-7
2. Claes A, Idema AJ, Wesseling P (2007) Diffuse glioma growth: a guerilla war. Acta Neuropathol 114(5):443–458. doi:10.1007/s00401-007-0293-7
3. Weller M, van den Bent M, Hopkins K, Tonn JC, Stupp R, Falini A, Cohen-Jonathan-Moyal E, Frappaz D, Henriksson R, Balana C, Chinot O, Ram Z, Reifenberger G, Soffietti R, Wick W (2014) EANO guideline for the diagnosis and treatment of anaplastic gliomas and glioblastoma. Lancet Oncol 15(9):e395–e403. doi:10.1016/s1470-2045(14)70011-7
4. Chang EL, Akyurek S, Avalos T, Rebueno N, Spicer C, Garcia J, Famiglietti R, Allen PK, Chao KS, Mahajan A, Woo SY, Maor MH (2007) Evaluation of peritumoral edema in the delineation of radiotherapy clinical target volumes for glioblastoma. Int J Radiat Oncol Biol Phys 68(1):144–150. doi:10.1016/j.ijrobp.2006.12.009
5. Oppitz U, Maessen D, Zunterer H, Richter S, Flentje M (1999) 3D-recurrence-patterns of glioblastomas after CT-planned postoperative irradiation. Radiother Oncol 53(1):53–57. doi:10.1016/s0167-8140(99)00117-6
6. Kuroiwa T, Ueki M, Chen Q, Suemasu H, Taniguchi I, Okeda R (1994) Biomechanical characteristics of brain edema: the difference between vasogenic-type and cytotoxic-type edema. Acta Neurochir Suppl (Wien) 60:158–161
7. Louis DN (2007) WHO classification of tumours of the central nervous system. World Health Organization. WHO Press, Geneva, Switzerland
8. Moenninghoff C, Maderwald S, Theysohn JM, Kraff O, Ladd ME, El Hindy N, van de Nes J, Forsting M, Wanke I (2010) Imaging of adult astrocytic brain tumours with 7 T MRI: preliminary results. Eur Radiol 20(3):704–713. doi:10.1007/s00330-009-1592-2
9. Christoforidis GA, Grecula JC, Newton HB, Kangarlu A, Abduljalil AM, Schmalbrock P, Chakeres DW (2002) Visualization of microvascularity in glioblastoma multiforme with 8-T high-spatial-resolution MR imaging. AJNR Am J Neuroradiol 23(9):1553–1556
10. Christoforidis GA, Yang M, Abduljalil A, Chaudhury AR, Newton HB, McGregor JM, Epstein CR, Yuh WT, Watson S, Robitaille PM (2012) "Tumoral pseudoblush" identified within gliomas at high-spatial-resolution ultrahigh-field-strength gradient-echo MR imaging corresponds to microvascularity at stereotactic biopsy. Radiology 264(1):210–217. doi:10.1148/radiol.12110799
11. Lupo JM, Li Y, Hess CP, Nelson SJ (2011) Advances in ultra-high field MRI for the clinical management of patients with brain tumors. Curr Opin Neurol 24(6):605–615. doi:10.1097/WCO.0b013e32834cd495
12. Dammann P, Kraff O, Wrede KH, Ozkan N, Orzada S, Mueller OM, Sandalcioglu IE, Sure U, Gizewski ER, Ladd ME, Gasser T (2011) Evaluation of hardware-related geometrical distortion in structural MRI at 7 Tesla for image-guided applications in neurosurgery. Acad Radiol 18(7):910–916. doi:10.1016/j.acra.2011.02.011
13. Cho ZH, Min HK, Oh SH, Han JY, Park CW, Chi JG, Kim YB, Paek SH, Lozano AM, Lee KH (2010) Direct visualization of deep brain stimulation targets in Parkinson disease with the use of 7-tesla magnetic resonance imaging. J Neurosurg 113(3):639–647. doi:10.3171/2010.3.jns091385
14. Duchin Y, Abosch A, Yacoub E, Sapiro G, Harel N (2012) Feasibility of using ultra-high field (7 T) MRI for clinical surgical targeting. PLoS One 7(5):e37328. doi:10.1371/journal.pone.0037328
15. Teeuwisse WM, Brink WM, Haines KN, Webb AG (2012) Simulations of high permittivity materials for 7 T neuroimaging and evaluation of a new barium titanate-based dielectric. Magn Reson Med 67(4):912–918. doi:10.1002/mrm.24176
16. Schenck JF (1996) The role of magnetic susceptibility in magnetic resonance imaging: MRI magnetic compatibility of the first and second kinds. Med Phys 23(6):815–850
17. Marques JP, Kober T, Krueger G, van der Zwaag W, Van de Moortele PF, Gruetter R (2010) MP2RAGE, a self bias-field corrected sequence for improved segmentation and T1-mapping at high field. Neuroimage 49(2):1271–1281. doi:10.1016/j.neuroimage.2009.10.002
18. Mugler JP 3rd, Brookeman JR (1990) Three-dimensional magnetization-prepared rapid gradient-echo imaging (3D MP RAGE). Magn Reson Med 15(1):152–157
19. Wrede KH, Johst S, Dammann P, Umutlu L, Schlamann MU, Sandalcioglu IE, Sure U, Ladd ME, Maderwald S (2012) Caudal image contrast inversion in MPRAGE at 7 Tesla: problem and solution. Acad Radiol 19(2):172–178. doi:10.1016/j.acra.2011.10.004
20. Marques JP, Gruetter R (2013) New developments and applications of the MP2RAGE sequence–focusing the contrast and high spatial resolution R1 mapping. PLoS One 8(7):e69294. doi:10.1371/journal.pone.0069294

21. O'Brien KR, Kober T, Hagmann P, Maeder P, Marques J, Lazeyras F, Krueger G, Roche A (2014) Robust T1-weighted structural brain imaging and morphometry at 7 T using MP2RAGE. PLoS One 9(6):e99676. doi:10.1371/journal.pone.0099676
22. Hurley AC, Al-Radaideh A, Bai L, Aickelin U, Coxon R, Glover P, Gowland PA (2010) Tailored RF pulse for magnetization inversion at ultrahigh field. Magn Reson Med 63(1):51–58. doi:10.1002/mrm.22167
23. Okubo G, Okada T, Yamamoto A, Kanagaki M, Fushimi Y, Okada T, Murata K, Togashi K (2015) MP2RAGE for deep gray matter measurement of the brain: a comparative study with MPRAGE. J Magn Reson Imaging. doi:10.1002/jmri.24960
24. Van de Moortele PF, Auerbach EJ, Olman C, Yacoub E, Ugurbil K, Moeller S (2009) T1 weighted brain images at 7 Tesla unbiased for Proton Density, T2* contrast and RF coil receive B1 sensitivity with simultaneous vessel visualization. Neuroimage 46(2):432–446. doi:10.1016/j.neuroimage.2009.02.009
25. Hennig J, Nauerth A, Friedburg H (1986) RARE imaging: a fast imaging method for clinical MR. Magn Reson Med 3(6):823–833
26. Mugler JP, Kiefer B, Brookeman JT (2000) Three-dimensional T2-weighted imaging of the brain using very long spin-echo trains. In: Proceedings of the 8th Scientific Meeting of the International Society for Magnetic Resonance in Medicine. Denver, Colorado, p 687
27. Mugler JP, Wald LL, Brookeman JR (2001) T2-weighted 3D spin-echo train imaging of the brain at 3 Tesla: reduced power deposition using low flip-angle refocusing RF pulses. In: Proceedings of the 9th Scientific Meeting of the International Society for Magnetic Resonance in Medicine. Glasgow, Scotland, p 438
28. Busse RF, Hariharan H, Vu A, Brittain JH (2006) Fast spin echo sequences with very long echo trains: design of variable refocusing flip angle schedules and generation of clinical T2 contrast. Magn Reson Med 55(5):1030–1037. doi:10.1002/mrm.20863
29. Schaap K, Christopher-de Vries Y, Mason CK, de Vocht F, Portengen L, Kromhout H (2014) Occupational exposure of healthcare and research staff to static magnetic stray fields from 1.5–7 T MRI scanners is associated with reporting of transient symptoms. Occup Environ Med 71(6):423–429. doi:10.1136/oemed-2013-101890
30. Heilmaier C, Theysohn JM, Maderwald S, Kraff O, Ladd ME, Ladd SC (2011) A large-scale study on subjective perception of discomfort during 7 and 1.5 T MRI examinations. Bioelectromagnetics 32(8):610–619. doi:10.1002/bem.20680
31. Ward BK, Roberts DC, Della Santina CC, Carey JP, Zee DS (2015) Vestibular stimulation by magnetic fields. Ann N Y Acad Sci 1343:69–79. doi:10.1111/nyas.12702
32. Brink WM, van der Jagt AM, Versluis MJ, Verbist BM, Webb AG (2014) High permittivity dielectric pads improve high spatial resolution magnetic resonance imaging of the inner ear at 7 T. Invest Radiol 49(5):271–277. doi:10.1097/rli.0000000000000026
33. Price RR, Axel L, Morgan T, Newman R, Perman W, Schneiders N, Selikson M, Wood M, Thomas SR (1990) Quality assurance methods and phantoms for magnetic resonance imaging: report of AAPM nuclear magnetic resonance Task Group No. 1. Med Phys 17(2):287–295
34. Lerski RA, Schad LR (1998) The use of reticulated foam in texture test objects for magnetic resonance imaging. Magn Reson Imaging 16(9):1139–1144
35. Wang D, Doddrell DM, Cowin G (2004) A novel phantom and method for comprehensive 3-dimensional measurement and correction of geometric distortion in magnetic resonance imaging. Magn Reson Imaging 22(4):529–542. doi:10.1016/j.mri.2004.01.008
36. Roue A, Ferreira IH, Van Dam J, Svensson H, Venselaar JL (2006) The EQUAL-ESTRO audit on geometric reconstruction techniques in brachytherapy. Radiother Oncol 78(1):78–83. doi:10.1016/j.radonc.2005.12.004
37. Kim HY, Lee SI, Jin SJ, Jin SC, Kim JS, Jeon KD (2014) Reliability of stereotactic coordinates of 1.5 and 3 T MRI in radiosurgery and functional neurosurgery. J Korean Neurosurg 55(3):136–141. doi:10.3340/jkns.2014.55.3.136
38. Walker A, Liney G, Metcalfe P, Holloway L (2014) MRI distortion: considerations for MRI based radiotherapy treatment planning. Australas Phys Eng Sci Med 37(1):103–113. doi:10.1007/s13246-014-0252-2
39. van Herk M (2004) Errors and margins in radiotherapy. Semin Radiat Oncol 14(1):52–64. doi:10.1053/j.semradonc.2003.10.003
40. Wang D, Strugnell W, Cowin G, Doddrell DM, Slaughter R (2004) Geometric distortion in clinical MRI systems Part II: correction using a 3D phantom. Magn Reson Imaging 22(9):1223–1232. doi:10.1016/j.mri.2004.08.014
41. Baldwin LN, Wachowicz K, Thomas SD, Rivest R, Fallone BG (2007) Characterization, prediction, and correction of geometric distortion in 3 T MR images. Med Phys 34(2):388–399
42. Schmidt MA, Payne GS (2015) Radiotherapy planning using MRI. Phys Med Biol 60(22):R323–R361. doi:10.1088/0031-9155/60/22/r323
43. Chang HC, Chuang TC, Lin YR, Wang FN, Huang TY, Chung HW (2013) Correction of geometric distortion in Propeller echo planar imaging using a modified reversed gradient approach. Quant Imaging Medicine Surg 3(2):73–81. doi:10.3978/j.issn.2223-4292.2013.03.05
44. Wang FN, Huang TY, Lin FH, Chuang TC, Chen NK, Chung HW, Chen CY, Kwong KK (2005) PROPELLER EPI: an MRI technique suitable for diffusion tensor imaging at high field strength with reduced geometric distortions. Magn Reson Med 54(5):1232–1240. doi:10.1002/mrm.20677